IEEE Robotics and Automation Letters (RA-L) paper, presented at ICRA 2024, Yokohama, Japan. Cite as RA-L paper.

Geared Rod-driven Continuum Robot with Woodpecker-inspired Extension Mechanism and IMU-based Force Sensing

Ujjal Mavinkurve[1], Ayato Kanada[1], Seyed Amir Tafrishi[2], Koki Honda[3], Yasutaka Nakashima[1], Motoji Yamamoto[1]

***Abstract*—Continuum robot arms that can access confined spaces are useful in many applications, such as invasive surgery, search and rescue, and inspection. However, their reach is often limited because their extension mechanism relies on elastic deformation or folding structures. To address this challenge, we propose a continuum robot with a novel extension mechanism inspired by the impressive ability of woodpeckers to extend and bend their long tongues to catch insects in tree holes. The proposed mechanism can change the effective length of the robot from almost zero to any length by moving the robot's body back and forth. Our prototype robot demonstrated a maximum extension of 450 mm and a minimum bending radius of 125 mm. In addition, we developed a Gaussian process regression model to predict an external force applied to the robot's tip using inertial measurement units. This enabled us to determine the magnitude and direction of the force with an error rate of 4.8 percent and 11.1 percent, even when the robot's length was varied between the training and test data. The unrestricted extension capability of the proposed approach has the potential to increase the application prospects of continuum robots.**

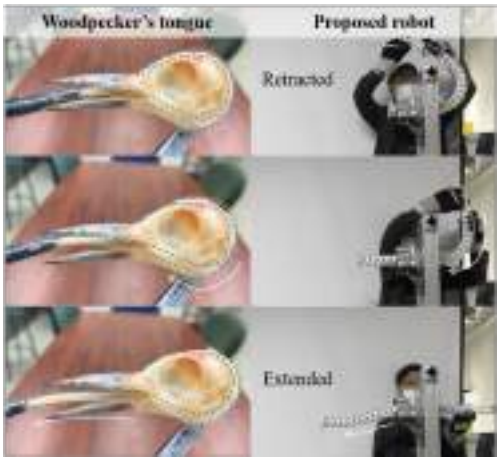

Fig. 1. Snapshot of the woodpecker's tongue [15] and the proposed robot in transition from the retracted position to the extended position.

I. Introduction

Continuum robots with extension and bending capabilities can navigate and explore confined spaces, and grasp and retrieve hard-to-reach targets. As a result, they have potential applications in minimally invasive surgery, search and rescue, and inspection [1], [2]. However, their reach is often limited by their extension mechanism, which relies on elastic deformation or folding structures. An ideal extension mechanism should change the effective length of the robot from zero to arbitrary length.

Several continuum robots with different extension mechanisms have been reported; however achieving both significant extension and bending is notable challenge. Pneumatic or hydraulic continuum robots are actuated by grouping three or more chambers in parallel [3], [4]. Selective inflation of the chambers enables the robot to both extend and bend; however the minimum/maximum length depends on the unpressurized/pressurized chamber length. Wire-driven continuum robots can also facilitate extension via a stretchable backbone [5], [6] or a concentric tube backbone [7]–[10]. The stretchable backbone (e.g., spring or origami) is a simple structure but the rate of expansion and contraction is limited owing to its constituent elastic materials and structure. Conversely, the concentric tube backbone provides high stiffness owing to its non-stretchable structure, but the maximum extension distance depends on the tube diameter. Growing robots achieve tip extension by pressurizing flexible, thin-walled tubes [11]. Although several steerable growing robots have been developed [12], [13], their extension is typically slow and irreversible. Another approach is to mount the entire continuum robot on a linear or rotary stage for pseudo-extension capability [14]. The moving stage is applicable to most continuum robots, but requires a large force to move the robot equipped with heavy motors. Moreover, the robot on the stage reduces its available degrees of freedom (DoF) in the workspace as the stage retracts and the robot length shortens.

Rod-driven continuum robots, whose extension mechanism is independent of elastic deformation or folding structures, can potentially be used to solve the aforementioned extension and bending problem. Their actuation mechanism uses linear motors to move multiple rods arranged in parallel to facilitate

Manuscript received: July, 8, 2023; Revised August, 31, 2023; Accepted October, 25, 2023.

This paper was recommended for publication by Editor Clement Gosselin upon evaluation of the Associate Editor and Reviewers' comments. This work was supported by JSPS KAKENHI Grant Number 22K14224, JST ACT-X Grant Number JPMJAX23K6, and Grant-in-Aid for JSPS Research Fellow (No. 23KJ1695). *(Corresponding author: Ayato Kanada)*

[1]Ujjal Mavinkurve, Ayato Kanada, Yasutaka Nakashima, Motoji Yamamoto are with the Department of Mechanical Engineering at Kyushu University, 744 Motooka, Nishi-ku, Fukuoka, 819-0395, Japan. m.ujjal, kanada, nakashima, yama@ce.mech.kyushu-u.ac.jp

[2]Seyed Amir Tafrishi is with Engineering School, Cardiff University, 5 The Parade, Newport Road, Queen's Buildings, Cardiff, CF24 3AA, Wales, UK. tafrishisa@cardiff.ac.uk

[3]Koki Honda is with Graduate School of Frontier Sciences at The University of Tokyo, 5-1-5, Kashiwanoha, Kashiwa, Chiba, 277-0882, Japan.khonda@edu.k.u-tokyo.ac.jp

Digital Object Identifier (DOI): see top of this page.

IEEE Robotics and Automation Letters (RA-L) paper, presented at ICRA 2024, Yokohama, Japan. Cite as RA-L paper.

IEEE Robotics and Automation Letters (RA-L) paper, presented at ICRA 2024, Yokohama, Japan. Cite as RA-L paper.

extension and bending motions. These motions depend on whether the relative positions of the rods are unconstrained or constrained (we call the former the unconstrained type and the latter the constrained type). The unconstrained type facilitates significant extension [16], but the lack of shape constraints among the rods can lead to unexpected twisting and nonlinear bending (nonconstant-curvature shapes). The constrained type uses disks with through holes connected by springs [17], [18]. The constraint provided by the disks facilitates large linear bending (constant-curvature shapes), but the spring's restoring force limits the extension. Additionally, the distance between the disks increases as the robot extends, and the constraint is reduced. Continuum robots intermediate between these two types have also been developed, but with similar problems [19], [20]. Therefore, a novel constraint mechanism that is independent of the robot's extension is required.

Inspired by woodpeckers, a novel rod-driven continuum robot capable of large extension and linear bending has been developed (Fig. 1). Woodpeckers have an excellent extensible elongated manipulator or tongue, that can catch small insects by navigating deep into tree holes [21], [22]. The tongue is supported by a series of small bones called hyoid bones, which prevent stretching but enable back-and-forth sliding during extension. Inspired by this sliding mechanism, we had earlier successfully demonstrated a prototype with a simple 2D extension mechanism concept [23], which has not been demonstrated in 3D [24]. In this report, we extend the 2D operation to 3D space. The new mechanism has two unique features, as shown in Fig 2. The first is a constraint mechanism, which is a chain of disks connected at a fixed distance, similar to hyoid bones. The disks constrain the rods to facilitate linear bending, regardless of the robot's extension. The other is a rack-and-pinion actuation system, which consists of a rotary motor that engages a rod using a linear gear. As the motor rotates, the gear rod slides back and forth together with the disks, allowing a large extension almost equal to the length of the robot. This sliding mechanism can change the effective length of the robot from almost zero to any arbitrary length.

Another challenge for continuum robots is force sensing. Accurate sensing of external forces is critical for enabling interaction with the environment, particularly for extensible continuum robots whose sensitivity to external forces changes with length. One major force estimation method is based on sensing the shape of the continuum robot under deflection [19], [25]–[29]. Shape or deflection of the continuum robot is measured using fiber Bragg grating sensors placed along the length of the continuum robot [25], [29], [30]. While Fiber Bragg sensors are an excellent solution for the small-scale of continuum robots working on a surgical scale, their non-linear characteristics and complex fabrication prohibit their application to larger-scale continuum robots. Another approach to shape-based force sensing is by using load cells attached to the base of the continuum robots along with mathematical models such as piecewise-constant curvature (PCC), Kirchoff theory and Cosserat theory [19], [26]–[28], [30], [31]. These methods have been either developed for surgical environments or have been proven only in simulation. For surgical environments, the size of the robot and scale of loading is much smaller than the proposed continuum robot's scale and intended application. Hence, the assumptions under

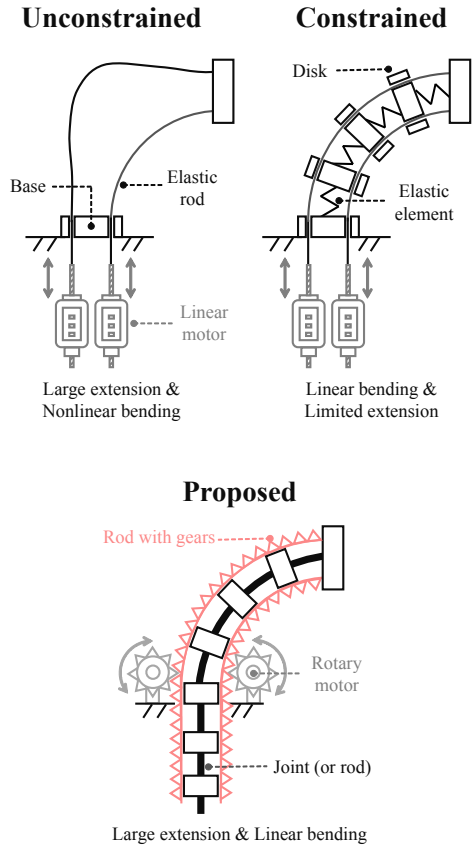

Fig. 2. Characteristics of rod-driven extensible continuum robots. The unconstrained type has a large extension but nonlinear bending. The constrained type has linear large bending but limited extension. The proposed robot combines the advantages of conventional unconstrained and constrained types.

which these methods were developed may not be applicable to the proposed continuum robot. Limited work has been found on development of force sensing methods for larger scale multi-backbone continuum robots.

In recent years, inertial measurement unit (IMU) sensors have attracted attention as highly reliable devices for pose and shape estimation of continuum robots [32], [33]. Combining the IMU-sensor information with the PCC model assumption enables modeling of continuum robots under external effects and more accurate feedback control.However, their application for multi-section model estimation and force sensing has not been well investigated.

There are two main contributions based on our work. First, we propose a novel woodpecker-inspired rod-driven continuum robot design that facilitates significant extension and bending. Second, we introduce a force sensing (determination) method using IMU sensors attached to the continuum robot. The incorporation of shape parameters determined by the IMU sensors into a Gaussian process (GP) regression yields the magnitude and direction of the force applied to the robot's tip. GP regression has been investigated previously for the modeling of soft robots [34], [35]. The authors in [34] trained local GP regression to learn inverse kinematics of a soft robot and detect the presence of external disturbances. A soft robot model capable of modeling uncertainties and external

IEEE Robotics and Automation Letters (RA-L) paper, presented at ICRA 2024, Yokohama, Japan. Cite as RA-L paper.

disturbances was developed using GP regression in [35]. While the previous literature shows the robustness of GP regression in modeling of soft robots under uncertainty, there has been limited research on its application for force estimation in soft robots. An advantage of this method is that the regression model predicts the tip force magnitude and direction for previously untrained observations after training.

II. Mechanical Design

A. Woodpecker tongue mechanism

This section describes the mechanism of operation of woodpecker tongues, which are excellent manipulators capable of extension and bending. The woodpecker tongue consists of the hyoid bones along associated connective tissues such as muscles and soft tissues (Fig. 3(a)). The hyoid bones begin in the nostril of the upper beak and travel over the top of the skull and around the back. The primary function of the hyoid bones is to support and allow for the extension of the tongue. When the muscles surrounding the relaxed hyoid bones contract, the hyoid bones wrap tightly around the skull, sliding its posterior end forward. The posterior end, which is not directly attached to the skull, can slide a large distance, allowing the tongue to extend up to three times as far as the beak. This sliding mechanism is advantageous for extensible continuum robots in two ways. One is to obtain a large extension distance and the other is to keep the distance between each hyoid bone constant.

B. Design overview

Our idea is to reproduce the operational mechanism of a woodpecker's tongue by considering the constraining disk as the hyoid bone. Fig. 3(b) shows the proposed robot that consists of a backbone passing through a motor unit with three DC motors. The backbone, inspired by the woodpecker, is not directly attached to the robot's base and can achieve large extensions while maintaining constant disk distances. The constraining disks support the geared rods to suppress nonlinear deformation, which allows the backbone to bend at large angles. The geared rod, with one end attached to a tip disk and the other end free, engages with a worm gear attached to the DC motor. Similar to the rack and pinion mechanism, rotating the worm gear moves the geared rod laterally with respect to the motor unit. The motor unit extends and bends the backbone by controlling each rod length. The backbone, inspired by the woodpecker, is not directly attached to the robot's base and can achieve large extensions while maintaining constant disk distances. Moreover, the backbone behind the motor unit can be rolled up and folded into a small space like the hyoid bone, as shown in Fig. 1. The following subsections describe the details of the constraining disk and the geared rod, which are the key elements of the proposed mechanism.

C. Constraining disk

The constraining disk prevents unexpected torsion and nonlinear deformation of the robot by maintaining the rod distances. Fig. 4(a) illustrates the front view of a single constraining disk and its insertion into the motor unit. This disk

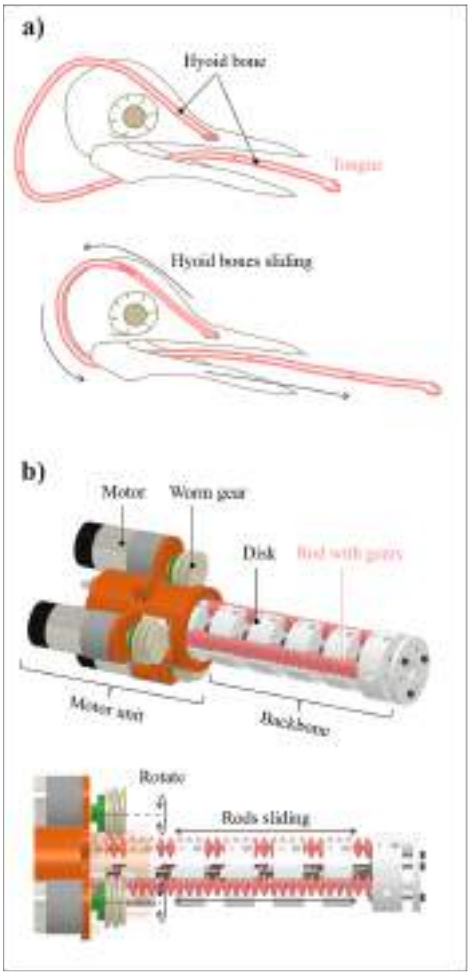

Fig. 3. Woodpecker-inspired extension mechanism. (a) The hyoid bones with the free end allow the woodpecker to extend its tongue. (b) The backbone with the free end allows the proposed mechanism to extend the backbone.

features three partially open holes through which the rods pass, with an angle of approximately 120°, which facilitates the transmission of power from the worm gear. The constraining disk also includes a concave hole situated between the two partially open holes, which fits onto a convex protrusion on the motor unit to prevent rotation of the backbone along the long axis. Fig. 4(b) shows a chain of disks connected by universal joints to maintain a constant disk distance. As an alternative to universal joints, an elastic rod can be used to connect the disks to reduce the weight; however, the chain will be vulnerable to torsion. This chain has a diameter of 34 mm, a disk width of 20 mm, and a disk distance of 13 mm.

D. Geared rod

The proposed geared rod acts as a flexible rack gear to bend the backbone in 3D. A flat rack gear that bends in 2D is commercially available, but none that bends in 3D exists to our knowledge. To make this, we first consider the tooth profile of a trapezoidal gear as shown in Fig. 5. One rotation of this tooth profile in the long-axis direction results in the form of a 3D rack gear. Next, we consider the manufacturing method of this gear. The length of the 3D rack gear should be

IEEE Robotics and Automation Letters (RA-L) paper, presented at ICRA 2024, Yokohama, Japan. Cite as RA-L paper.

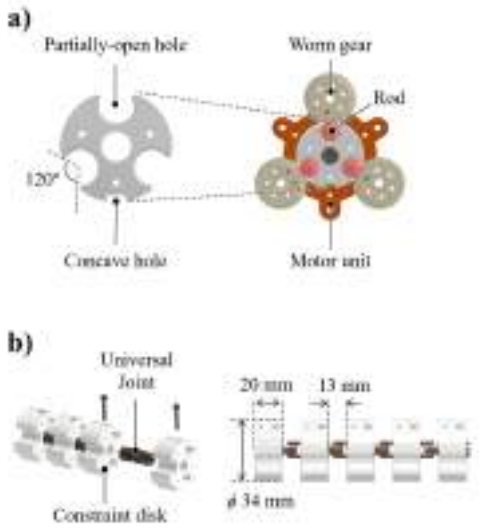

Fig. 4. (a) Front view of a single constraining disk and its insertion into the motor unit. (b) Chain of disks connected by universal joints to maintain a constant disk distance

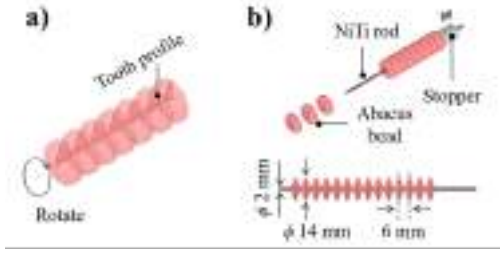

Fig. 5. (a) Concept of a geared rod acting as a 3D bendable rack gear. Rotating the tooth profile of a trapezoidal gear along the longitudinal axis results in the shape of the 3D rack. (b) To create this shape, a nickel–titanium (NiTi) rod and 3D-printed abacus beads were used.

adjustable to fit the robot's length. Thus, we proposed the gear rod that consists of a nickel-titanium (NiTi) rod as the core shaft and 3D-printed abacus beads as the gears. Increasing the number of abacus beads can lengthen the rack gear. Another advantage of gear rods is that the use of rotary motors instead of linear motors can provide greater travel distances without motor stroke limitations.

III. Modeling

A. Overview

We briefly describe the model validation force sensing approach based on the deformation of the continuum robot (Fig. 6). The continuum robot is fixed to the base with an arbitrary initial shape. IMU sensors and motion capture markers are placed on the disks along the length of the continuum robot. The IMU sensors measure the bending angles at discrete points along the continuum robot. The angle data is used as an input along with the motor encoder data to determine the parameters of PCC model assumption to determine the robot's shape. For the validation of this model, the position estimated by the IMU-based PCC model and the motion capture markers is compared for arbitrary shapes of the continuum robot. For

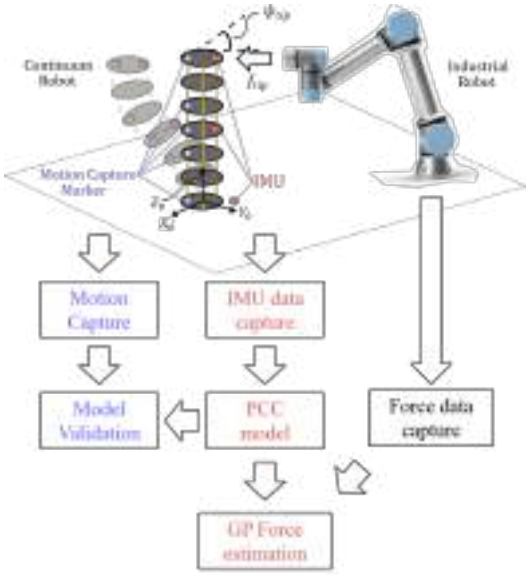

Fig. 6. Overview of the model validation and force sensing approach. IMU sensors (in red) and motion capture markers (in blue) placed on the body of the continuum robot to determine its shape. IMU sensors under the PCC model assumption determine the full shape of the continuum robot.

the force estimation approach, the industrial robot pushes and deforms the continuum robot with a specific force in a given direction. The magnitude of the applied force is denoted as f_{tip}, and the angle of this force with respect to the Y-axis of the base frame is denoted as ψ_{tip}. While the continuum deforms, the parameters of the PCC model are recorded based on the change in IMU sensor's angles. A GP regression model was built using f_{tip}, ψ_{tip}, and the robot's shape to estimate the applied forces based on the IMU data. This GP regression model was derived from experiments using three different initial shapes for application to the continuum robot with different shapes and lengths.

B. Piece-wise constant curvature (PCC) model

Here, we determine the shape of the continuum robot using a PCC model based on the IMU data. The PCC model consists of smoothly connected arcs of constant curvature. Let us consider a PCC model with n segments. The i^{th} segment of the PCC contains the curvature κ_i, the angle of the arc in the bending plane θ_i, and the angle the arc makes with the x-axis of the coordinate system at the base of the arc ϕ_i, as shown in Fig. 7(a). We compute the parameters of these arcs using the orientation data obtained from the IMU sensors attached at the disks along the length of the manipulator, as shown in Fig. 7(b).

From the i^{th} and the $i-1^{th}$ IMU, we obtain the orientation data in the form of the rotation matrix $\mathbf{R}_g^i$ and $\mathbf{R}_g^{i-1}$, where g denotes the ground frame. To calculate the PCC parameters of the i^{th} segment $[\kappa_i, \theta_i, \phi_i]$, the rotation matrix between the i^{th} IMU and the $i-1^{th}$ IMU $\mathbf{R}_{i-1}^i$ is used, which is written as follows:

$$\mathbf{R}_{i-1}^i = \begin{bmatrix} R_{11} & R_{12} & R_{13} \\ R_{21} & R_{22} & R_{23} \\ R_{31} & R_{32} & R_{33} \end{bmatrix}. \quad (1)$$

IEEE Robotics and Automation Letters (RA-L) paper, presented at ICRA 2024, Yokohama, Japan. Cite as RA-L paper.

IEEE Robotics and Automation Letters (RA-L) paper, presented at ICRA 2024, Yokohama, Japan. Cite as RA-L paper.

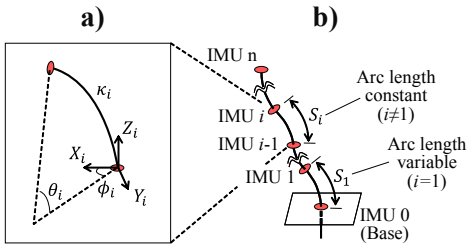

Fig. 7. PCC modeling of the extensible continuum robot. a) Kinematic description of the i^{th} segment. b) The continuum robot has $n+1$ IMUs, divided into n segments. Note that as the robot extends and retracts, the number of IMUs used and the arc length closest to the base change.

We obtain the rotation matrix $\mathbf{R}^i_{i-1}$ by post multiplying the inverse of $\mathbf{R}^{i-1}_g$ with $\mathbf{R}^i_g$ as shown below,

$$\mathbf{R}^i_{i-1} = \mathbf{R}^i_g \mathbf{R}^g_{i-1} \tag{2}$$

We obtain the rotation matrix between each i^{th} PCC segment using the preceding equation. Referring to Eq. (2) for the rotation matrix $\mathbf{R}^i_{i-1}$, i^{th} segments, the PCC parameters $[\kappa_i, \theta_i, \phi_i]$ are given by

$$\begin{aligned} \theta_i &= \cos^{-1} R_{33}, \\ \phi_i &= \tan^{-1}\left(\frac{R_{23}}{R_{33}}\right), \\ \kappa_i &= \frac{\theta_i}{s_i}. \end{aligned} \tag{3}$$

where R_{33} and R_{23} denote the element in the 3^{rd} row and 3^{rd} column and the 2^{nd} row and 3^{rd} column of the matrix $(\mathbf{R}^i_{i-1})$ respectively. Please note that $\tan^{-1}$ is the 2-argument inverse tangent atan2 function; s_i is the arc length of the i^{th} PCC segment. The arc length between the IMU sensors positioned on the disks of the continuum robot is constant as the robot extends or retracts. However, the arc length of the first PCC segment s_i changes during these processes. The arc length s_i is computed as follows,

$$s_i = \begin{cases} d, & \text{if } i = 2, .., n, \\ L - nd, & \text{if } i = 1 \end{cases} \tag{4}$$

where d is the constant distance between the IMU sensors, L is the total length of the continuum robot, and n is the number of PCC segments. L is expressed using each geared rod length L_1, L_2, and L_3 as follows:

$$L = \frac{L_1 + L_2 + L_3}{3} \tag{5}$$

C. Force determination

Using the shape parameters of the continuum robot defined in the previous section, we built independent Gaussian process regression (GP) models to determine the magnitude f_{tip} and direction of the tip force ψ_{tip}. We used the lengths of the geared rods $[L_1, L_2, L_3]$ and the PCC parameters of the last segment $[\kappa_n, \theta_n, \phi_n]$ as inputs of the regression model. For the present case, we estimate the tip force on the continuum robot. Hence, we consider the PCC parameters of the last segment of the PCC model for tip force estimation along with the geared rod lengths. This assumption is further justified by stating that the stiffness of the proposed continuum robot is high closer to the base as seen from the change in the bending angles of the first section of the PCC model with $\theta_1 = [-2.5^o, 10.7^o]$ and $\phi_1 = [-4.2, 3.5^o]$ and, its change in PCC parameters can be neglected. However, for longer lengths and more complex shape deformations, multiple sections of PCC may be considered as input. For the training set, the input $x = [\kappa_n, \theta_n, \phi_n, L_1, L_2, L_3]$ and output $y = [f_{tip}, \psi_{tip}]$ satisfy the following equation

$$y = G(x) + \varepsilon \tag{6}$$

where $G(x)$ is the Gaussian process function with a zero mean function and a covariance function $k(x_i, x_j)$; ε is white Gaussian noise with zero mean and variance σ^2_N. The covariance function $k(x_i, x_j)$ is a customized function. We used the standard squared-exponential kernel function [36] in the proposed application:

$$k(x_i, x_j) = -\sigma_f^2 \exp\left[\frac{1}{2}\frac{(x_i - x_j)^T(x_i - x_j)}{\sigma_l^2}\right] \tag{7}$$

where $[\sigma_N, \sigma_f, \sigma_l]$ are hyper-parameters that can be found using standard optimization methods without the need for initialization or manual tuning of these parameters. The joint distribution of the training output y_s and the prediction y^*_s for the query input x^* using the trained model based on Eq. (6) is given by

$$\begin{bmatrix} y_s \\ y^*_s \end{bmatrix} \sim \mathcal{N}\left(0, \begin{bmatrix} k(x_i, x_j) + \sigma^2_N I & k(x_i, x^*_j) \\ k(x^*_i, x_j) & k(x^*_i, x^*_j) \end{bmatrix}\right) \tag{8}$$

where I is the identity matrix. We used the MATLAB function "fitrgp" in the statistical and machine learning toolbox for training and prediction of the GP regression. For hyper-parameter optimization, the function "fminunc" in MATLAB's optimization toolbox was used.

Fig. 8. PCC validation experiment. Motion capture markers (in blue) and IMU sensors(in red) are placed along the length of the continuum robot. For case 2, a weight is placed at the tip of the continuum robot.

IV. Experiment

A. Model Validation experiment

The different conditions for which the PCC model is validated is shown in Fig. 8. The continuum robot is placed horizontally with respect to the floor, to deform it naturally under the influence of gravity and two conditions are considered. In the first case shown in Fig. 8, the continuum robot is unloaded and deforms under gravity effect. In the second case shown in Fig. 8, a 250g weight is attached to the continuum robot's tip. For each case, the IMU sensors and motion capture data is recorded 10 times. The continuum robot is disturbed and brought back to position before each measurement. The

IEEE Robotics and Automation Letters (RA-L) paper, presented at ICRA 2024, Yokohama, Japan. Cite as RA-L paper.

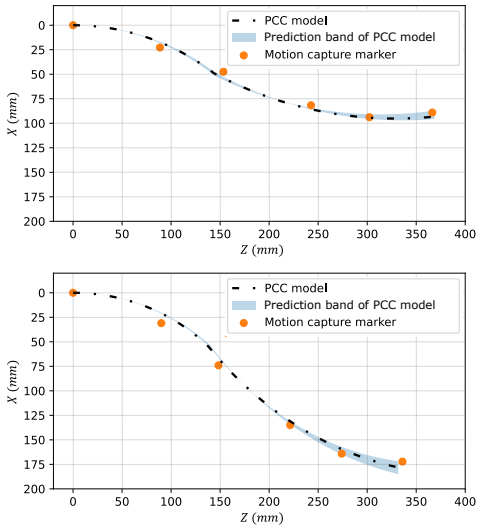

Fig. 9. Results of the PCC validation experiment shown in X-Z plane. Dashed black line shows the PCC model estimated by the average of PCC parameters. Orange markers show the motion capture marker points. The plot on top shows results for case 1 and the bottom plot shows results for case 2.

Fig. 10. Experimental setup for force prediction using GP. An industrial robot with force sensors pushed the tip of the continuum robot with IMU sensors from different angles ψ_{tip} and the tip force f_{tip} was recorded.

IMU sensor data is used to model the continuum robot under the PCC assumption as two arcs. The comparison of the IMU-based PCC model and motion capture markers has been illustrated in Fig. 9. The results have been shown in the X-Z plane as the continuum robot deforms only in the X-Z plane. The average of the estimated PCC model is shown by the black dotted line and the prediction band is shown in blue. The motion capture markers have been shown by orange markers. From the results, the IMU-based PCC model predicts the shape of the continuum robot with a maximum error of 1.4% by length in case 1 and 3.8% by length in case 2. The results show that multi-segment IMU-based PCC model can be used to estimate the shape of continuum manipulators with good accuracy under external effects.

B. Force determination experiment

Fig. 10 shows the experimental setup for training and testing of the GP regression model defined by Eqs. (6)–(8). When the continuum robot is placed horizontally with respect to the floor, it deforms naturally under the influence of gravity. The continuum robot has one IMU sensor on the robot's base and two IMU sensors on the disks along the length of the robot. The orientation angles from these IMU sensors is used to estimate the shape of the continuum using a two-segment PCC model. An industrial robot (UR5e) was used to push the tip of the continuum robot approximately 100 mm from the direction ψ_{tip}. The continuum robot tip had a hemispherical attachment to ensure smooth contact with the industrial robot. The industrial robot with force sensors estimated the pushing force f_{tip} based on the reaction force of the continuum robot. We prepared four versions of the continuum robot with different shapes as shown in Fig. 11; cases 1–3 were used as training data and case 4 was used as test data. For the training data, the magnitude of the force f_{tip} was recorded three times while changing its direction ψ_{tip} from -90^o to 90^o in steps of 30^o. For the test data, the magnitude of the force f_{tip} was recorded three times while changing its direction ψ_{tip} from -90^o to 90^o in steps of 45^o. The difference in test and training data was used to evaluate the accuracy of GP regression for untrained conditions.

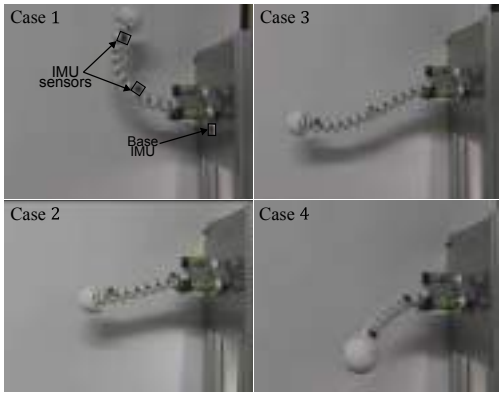

Fig. 11. Four cases of the continuum robot with different lengths of gear rods for the experiment in Fig.9. The geared rod lengths for each case are shown in Table I. Cases 1–3 were used as training data, and case 4 was used as the test data.

We use the PCC model to approximate the shape of the continuum robot as two arcs. The second segment of PCC parameters $[\kappa_2, \theta_2, \phi_2]$ and the lengths of the continuum robot $[L_1, L_2, L_3]$ were used as the inputs of the GP regression model. The training of the GP regression model for the magnitude of the tip force f_{tip} and the angle of tip force ψ_{tip} was performed independently using data obtained from training cases 1–3. The accuracy of the two GP regression models was tested using the data obtained from case 4. Fig. 12 shows the actual tip force and the error between the actual tip force and the predicted GP force. A scatter plot of the tip force obtained based on the experiments for the test case as a function of the

TABLE I
LENGTH OF GEARED RODS USED FOR THE EXPERIMENT

Case	L (mm)	L_1 (mm)	L_2 (mm)	L_3 (mm)
1	394	420	342	420
2	253	253	253	253
3	462	462	462	462
4	306	282	318	318

IEEE Robotics and Automation Letters (RA-L) paper, presented at ICRA 2024, Yokohama, Japan. Cite as RA-L paper.

IEEE Robotics and Automation Letters (RA-L) paper, presented at ICRA 2024, Yokohama, Japan. Cite as RA-L paper.

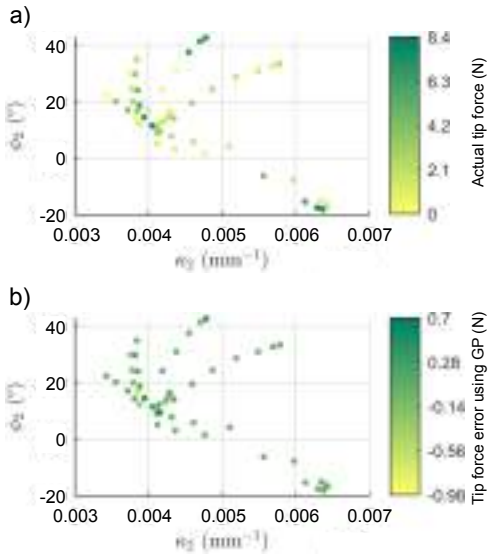

Fig. 12. Scatter plot of a) actual tip force obtained from the experiment. b) Error between the actual tip force and the force predicted using the GP regression as a function of the bending angle ϕ_2 and curvature κ_2 of the second segment of the PCC for test case 4.

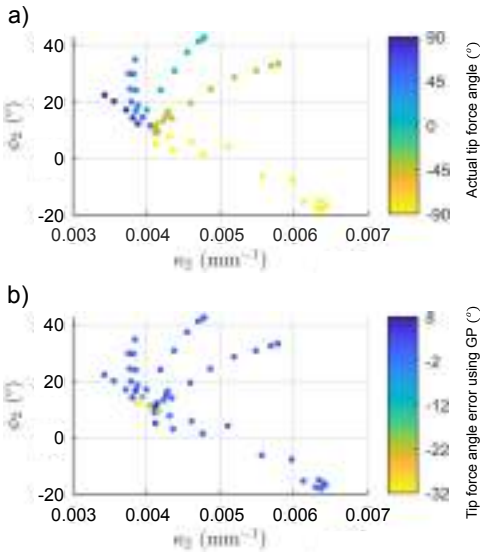

Fig. 13. Scatter plot of a) actual tip force angle obtained experimentally. b) Error between the actual tip force angle and the angle predicted via GP regression as a function of the bending angle ϕ_2 and curvature κ_2 of the second segment of the PCC for test case 4.

curvature κ_2 and bending angle ϕ_2 of the second segment of the PCC model is shown in Fig. 12(a). The continuum robot in its initial state has PCC parameters with a mean value of $[0.004\ \text{mm}^{-1}, 10^o]$. As the continuum robot deforms, the data points move radially outward with an increasing tip force, which has a maximum force of 8.2 N. The tip force exhibits significant variations based on the deformation direction of the continuum robot, which suggests that the stiffness of the robot changes according to the deformation direction. As depicted in Fig. 12(b), the force prediction error remains below 0.1 N for the majority of the input values, with a maximum error of approximately 1.0 N. The largest error of the tip force occurs near the continuum robot's initial state, characterized by a curvature of 0.004 mm^{-1} and a bending angle of 17°. The GP regression model considers neighboring data points to estimate the output force. However, in the initial state of the continuum robot, the direction of deformation is not known, resulting in an increased prediction error of the tip force. The tip force RMSE for the training data is 8.7 % of the average tip force and decreases to 4.8 % of the average tip force of the test case. The tip force angle variation from 90° to -90° in steps of 45° as a function of the curvature κ_2 and the bending angle ϕ_2 is shown in Fig. 13(a). The error in the tip force angle for the test case is shown in Fig. 13(b). Similar to the tip force prediction error, the tip force angle prediction error is a maximum at approximately the initial state of the continuum robot for a curvature of 0.0039 mm$^-1$, a bending angle of 12°, and a tip force angle of 90°. The error of the force tip angle is less than 2° on average with an RMSE of 11.8 % of the average for the training cases. The tip force angle prediction RMSE for the training case decreased slightly to 11.1 %.

C. Demonstration

In this section, we present two demonstrations that facilitate an intuitive understanding of the advantages of the proposed extension mechanism. The left image in Fig. 14 shows the proposed robot performing extension by rotating three motors at the same speed. The robot changed the effective length from 0 mm to 450 mm in 12 s. The right image in Fig. 14 shows the bending of the proposed robot via rotation of the three motors at different speeds. The robot was able to bend with a minimum radius of 125 mm. This minimum bending radius remained constant as the robot length changed because the

Fig. 14. Snapshot of the proposed robot during extension and bending. The robot can extend from a length of almost 0 mm up to 450 mm and can bend with a minimum bending radius of 125 mm.

TABLE II
RESULTS OF THE TIP FORCE AND ANGLE DETERMINATION MODEL

Output Parameters	Training RMSE (% of avg.)	Test RMSE (% of avg.)
f_{tip}	8.7%	4.8%
ψ_{tip}	11.8%	11.1%

IEEE Robotics and Automation Letters (RA-L) paper, presented at ICRA 2024, Yokohama, Japan. Cite as RA-L paper.

extension mechanism kept the disk distance constant.

V. Conclusion

To develop a continuum robot with large extension and bending ranges, we built a rod-driven continuum robot with a woodpecker-inspired extension mechanism. The proposed prototype exhibited a maximum extension of 450 mm and a minimum bending radius of 125 mm. Furthermore, a method for shape and force determination was developed by utilizing an industrial robot and IMU sensors. By training a Gaussian process regression model using an IMU-sensor-based PCC model and the lengths of the rods as the input, it was possible to determine the tip force magnitude and direction of the untrained shape of the continuum robot with an acceptable margin of error.

In our study, there are several points that need to be improved. First, the diameter of the geared rods is larger than that of simple rods and wires, increasing friction losses and robot diameter. Optimizing the gear geometry would allow us to develop rods with smaller diameters. Second, the proposed robot has only three degrees of freedom (DoF), which provides simple manipulation. Increasing the DoF requires to insert an additional motor unit into the backbone or to increase the number of geared rods held by the constraining disk. The former method allows for a smaller diameter design of the robot, while the latter method allows all motors to be installed on the base.

References

[1] P. K. Singh and C. M. Krishna, "Continuum arm robotic manipulator: A review," *Universal Journal of Mechanical Engineering*, vol. 2, no. 6, pp. 193–198, 2014.

[2] T. da Veiga, J. H. Chandler, P. Lloyd, G. Pittiglio, N. J. Wilkinson, A. K. Hoshiar, R. A. Harris, and P. Valdastri, "Challenges of continuum robots in clinical context: A review," *Progress in Biomedical Engineering*, vol. 2, no. 3, p. 032003, 2020.

[3] A. Bartow, A. Kapadia, and I. D. Walker, "A contractor muscle based continuum trunk robot," *International Journal of Systems Applications, Engineering & Development*, vol. 8, no. 198-206, p. 24, 2014.

[4] T. Ranzani, G. Gerboni, M. Cianchetti, and A. Menciassi, "A bioinspired soft manipulator for minimally invasive surgery," *Bioinspiration & biomimetics*, vol. 10, no. 3, p. 035008, 2015.

[5] J. Santoso and C. D. Onal, "An origami continuum robot capable of precise motion through torsionally stiff body and smooth inverse kinematics," *Soft Robotics*, vol. 8, no. 4, pp. 371–386, 2021.

[6] M. B. Wooten and I. D. Walker, "Vine-inspired continuum tendril robots and circumnutations," *Robotics*, vol. 7, no. 3, p. 58, 2018.

[7] Y. Zhang, H. Sun, Y. Jia, D. Huang, R. Li, Z. Mao, Y. Hu, J. Chen, S. Kuang, J. Tang *et al.*, "A continuum robot with contractible and extensible length for neurosurgery," in *2018 IEEE 14th International Conference on Control and Automation (ICCA)*. IEEE, 2018, pp. 1150–1155.

[8] I. D. Walker, D. Nahar, S. Verma, M. B. Wooten, and A. D. Kapadia, "Challenges in creating long continuum robots," in *2016 21st International Conference on Methods and Models in Automation and Robotics (MMAR)*, 2016, pp. 339–344.

[9] E. Amanov, J. Granna, and J. Burgner-Kahrs, "Toward improving path following motion: Hybrid continuum robot design," in *IEEE International Conference on Robotics and Automation*, 2017, pp. 4666–4672.

[10] T.-D. Nguyen and J. Burgner-Kahrs, "A tendon-driven continuum robot with extensible sections," in *2015 IEEE/RSJ International Conference on Intelligent Robots and Systems (IROS)*. IEEE, 2015, pp. 2130–2135.

[11] E. W. Hawkes, L. H. Blumenschein, J. D. Greer, and A. M. Okamura, "A soft robot that navigates its environment through growth," *Science Robotics*, vol. 2, no. 8, p. eaan3028, 2017.

[12] T. Takahashi, K. Tadakuma, M. Watanabe, E. Takane, N. Hookabe, H. Kajiahara, T. Yamasaki, M. Konyo, and S. Tadokoro, "Eversion robotic mechanism with hydraulic skeletonto realize steering function," *IEEE Robotics and Automation Letters*, vol. 6, no. 3, pp. 5413–5420, 2021.

[13] A. Sadeghi, A. Mondini, and B. Mazzolai, "Toward self-growing soft robots inspired by plant roots and based on additive manufacturing technologies," *Soft robotics*, vol. 4, no. 3, pp. 211–223, 2017.

[14] A. Mohammad, M. Russo, Y. Fang, X. Dong, D. Axinte, and J. Kell, "An efficient follow-the-leader strategy for continuum robot navigation and coiling," *IEEE Robotics and Automation Letters*, vol. 6, no. 4, pp. 7493–7500, 2021.

[15] WitmerLab, "Random act of anatomy - woodpecker hyolingual (tongue) apparatus," YouTube, February 2023. [Online]. Available: https://youtu.be/qfGXkNUIocc

[16] C. E. Bryson and D. C. Rucker, "Toward parallel continuum manipulators," in *2014 IEEE International Conference on Robotics and Automation (ICRA)*, 2014, pp. 778–785.

[17] A. L. Orekhov, V. A. Aloi, and D. C. Rucker, "Modeling parallel continuum robots with general intermediate constraints," in *2017 IEEE International Conference on Robotics and Automation (ICRA)*. IEEE, 2017, pp. 6142–6149.

[18] J. A. Childs and C. Rucker, "Leveraging geometry to enable high-strength continuum robots," *Frontiers in Robotics and AI*, vol. 8, p. 629871, 2021.

[19] R. Roy, L. Wang, and N. Simaan, "Modeling and estimation of friction, extension, and coupling effects in multisegment continuum robots," *IEEE/ASME Transactions on Mechatronics*, vol. 22, no. 2, pp. 909–920, 2016.

[20] G. Wu and G. Shi, "Design, modeling, and workspace analysis of an extensible rod-driven parallel continuum robot," *Mechanism and Machine Theory*, vol. 172, p. 104798, 2022.

[21] W. J. Bock, "Functional and evolutionary morphology of woodpeckers," *Ostrich*, vol. 70, no. 1, pp. 23–31, 1999.

[22] J.-Y. Jung, S. E. Naleway, N. A. Yaraghi, S. Herrera, V. R. Sherman, E. A. Bushong, M. H. Ellisman, D. Kisailus, and J. McKittrick, "Structural analysis of the tongue and hyoid apparatus in a woodpecker," *Acta biomaterialia*, vol. 37, pp. 1–13, 2016.

[23] R. Matsuda, U. K. Mavinkurve, A. Kanada, K. Honda, Y. Nakashima, and M. Yamamoto, "A woodpecker ' s tongue-inspired, bendable and extendable robot manipulator with structural stiffness," *IEEE Robotics and Automation Letters*, vol. 7, no. 2, pp. 3334–3341, 2022.

[24] ——, "Design of 3d-printed flexible robotic arm with bendable and extendable capacity," in *2023 IEEE/SICE International Symposium on System Integration (SII)*, 2023, pp. 1–5.

[25] Q. Qiao, D. Willems, G. Borghesan, M. Ourak, J. De Schutter, and E. Vander Poorten, "Estimating and localizing external forces applied on flexible instruments by shape sensing," in *2019 19th International Conference on Advanced Robotics (ICAR)*. IEEE, 2019, pp. 227–233.

[26] J. Back, T. Manwell, R. Karim, K. Rhode, K. Althoefer, and H. Liu, "Catheter contact force estimation from shape detection using a real-time cosserat rod model," in *2015 IEEE/RSJ International Conference on Intelligent Robots and Systems (IROS)*. IEEE, 2015, pp. 2037–2042.

[27] D. C. Rucker and R. J. Webster, "Deflection-based force sensing for continuum robots: A probabilistic approach," in *2011 IEEE/RSJ International Conference on Intelligent Robots and Systems*. IEEE, 2011, pp. 3764–3769.

[28] R. Yasin and N. Simaan, "Joint-level force sensing for indirect hybrid force/position control of continuum robots with friction," *The International Journal of Robotics Research*, vol. 40, no. 4-5, pp. 764–781, 2021.

[29] R. Xu, A. Yurkewich, and R. V. Patel, "Curvature, torsion, and force sensing in continuum robots using helically wrapped fbg sensors," *IEEE Robotics and Automation Letters*, vol. 1, no. 2, pp. 1052–1059, 2016.

[30] K. Xu and N. Simaan, "An investigation of the intrinsic force sensing capabilities of continuum robots," *IEEE Transactions on Robotics*, vol. 24, no. 3, pp. 576–587, 2008.

[31] R. J. Webster III and B. A. Jones, "Design and kinematic modeling of constant curvature continuum robots: A review," *The International Journal of Robotics Research*, vol. 29, no. 13, pp. 1661–1683, 2010.

[32] N. Lin, P. Wu, M. Wang, J. Wei, F. Yang, S. Xu, Z. Ye, and X. Chen, "Imu-based active safe control of a variable stiffness soft actuator," *IEEE Robotics and Automation Letters*, vol. 4, no. 2, pp. 1247–1254, 2019.

[33] J. Hughes, F. Stella, C. D. Santina, and D. Rus, "Sensing soft robot shape using imus: An experimental investigation," in *Experimental Robotics: The 17th International Symposium*. Springer, 2021, pp. 543–552.

[34] G. Fang, X. Wang, K. Wang, K.-H. Lee, J. D. Ho, H.-C. Fu, D. K. C. Fu, and K.-W. Kwok, "Vision-based online learning kinematic control for soft robots using local gaussian process regression," *IEEE Robotics and Automation Letters*, vol. 4, no. 2, pp. 1194–1201, 2019.

[35] D. Kim, M. Park, and Y.-L. Park, "Probabilistic modeling and bayesian filtering for improved state estimation for soft robots," *IEEE Transactions on Robotics*, vol. 37, no. 5, pp. 1728–1741, 2021.

[36] C. K. Williams and C. E. Rasmussen, *Gaussian processes for machine learning*. MIT press Cambridge, MA, 2006, vol. 2, no. 3.

IEEE Robotics and Automation Letters (RA-L) paper, presented at ICRA 2024, Yokohama, Japan. Cite as RA-L paper.